frontiers | Frontiers in Mechanical Engineering

TYPE Original Research
PUBLISHED 21 January 2026
DOI 10.3389/fmech.2025.1651334

OPEN ACCESS

EDITED BY
Stanislav N. Gorb,
University of Kiel, Germany

REVIEWED BY
Arash Shams Taleghani,
Ministry of Science, Research and Technology, Iran
Bin Yang,
Xi'an Jiaotong University, China

*CORRESPONDENCE
Cetin Canpolat,
ccanpolat@cu.edu.tr

RECEIVED 21 June 2025
REVISED 25 November 2025
ACCEPTED 05 December 2025
PUBLISHED 21 January 2026

CITATION
Tatlisoz MM and Canpolat C (2026) Fluid flow and mass transport along a microchannel with physics-informed neural networks.
Front. Mech. Eng. 11:1651334.
doi: 10.3389/fmech.2025.1651334

Fluid flow and mass transport along a microchannel with physics-informed neural networks

Mehmet Melih Tatlisoz and Cetin Canpolat*

Biomedical Engineering Department, Faculty of Engineering, Cukurova University, Adana, Türkiye

Introduction: In the present study, fluid and mass transport along a microchannel are aimed to be solved using physics-informed neural networks (PINN), which is an emerging solution method for partial differential equations (PDEs). For verification purposes, the same cases under identical conditions are modeled with a solver for finite element analysis (FEA), COMSOL Multiphysics.

Materials and methods: Continuity, Navier-Stokes, and Nernst-Planck Equations, which characterize momentum and mass conservation, are solved simultaneously by PINN as well as COMSOL Multiphysics. The problems are defined as steady or time-dependent with varying Reynolds numbers in the interval of $5 \times 10^{-6} \leq Re \leq 5 \times 10^{-2}$. The fluid is flowed by either pressure-driven or electrokinetically-driven. PDEs are nondimensionalized by scaling the quantities for PINN solving on the purpose of alleviating the computational burden. In contrast to usual approach, where the pressure scale is viscosity multiplied by the velocity scale divided by the length scale, pressure scale is determined as its maximum value.

Results and discussion: Calculation errors of PINN solver are observed as reasonably low, such as 3.04×10^{-5}, 4.76×10^{-3}, 3.60×10^{-4}, 6.02×10^{-3} for steady pressure-driven flow, time-dependent pressure-driven flow, steady electroosmotic flow, and time-dependent electroosmotic flow, respectively. To reduce the error margin at these values, pressure scale must be defined as the maximum pressure value. Therefore, the results of the FEA solver exhibit excellent overlap with the data obtained from PINN. For PINN, species concentrations of 0.52–1.75–2.71–3.36 mol/m^3 are accumulated at the outlet under pressure-driven flow for time points 50–100–150–200 seconds, respectively. Under electrokinetic flow, species concentrations are varied as 0.72–1.93–2.83–3.46 mol/m^3 for the same time points, respectively. In consideration of FEA, species concentrations are calculated as 0.52–1.75–2.71–3.39 mol/m^3 and 0.55–1.85–2.84–3.52 mol/m^3 under similar conditions for pressure-driven and electroosmotic flows, respectively.

Conclusion: Both Navier-Stokes and Nernst-Planck Equations can be solved with PINN in a single model, regardless of the flow generation method and the time dependency of the model. Because nearly identical calculations are carried out by the FEA solver. As a result, PINN is a notable alternative for simultaneous modeling of the flow and mass transport under pressure-driven and electrokinetic conditions for microfluidic applications.

KEYWORDS

microfluidics, physics-informed neural network, Navier-Stokes equation, nernst-planck equation, electrokinetics

1 Introduction

Fluid flow is a prominent component in many engineering applications, such as micro-nanofluidic chips (Canpolat et al., 2013a), hemodialysis (Abohtyra et al., 2019), etc. Therefore, a significant effort is made to understand the complex nature of the fluid flow. For instance, flow in the progressing cavity pumps (Al-Safran et al., 2017), viscous flow in a pressure-swirl atomizer (Laurila et al., 2019), flow along the obstructed airway (Tsuboi et al., 2019), multiphase flow in porous media (Lauser et al., 2011), etc. Countless analyses in this field are conducted *in silico* media due to relatively low costs, rapid results, and quantitative insight for the proposed designs. Navier-Stokes and Continuity equations are mainly used to solve fluid flow from the point of view of the continuum. If diluted chemical species are in action within the fluid medium, the Nernst-Planck Equation is generally incorporated into the model to understand different transport mechanisms of the dissolved chemical species, such as diffusion, convection, and electromigration. The fluids are conventionally mobilized with pressure differences across the channels. However, some significant disadvantages are attributed to the pressure-driven flow systems. The parabolic flow profile is effective in the flowing domain, which attenuates control over the emerging flow. Moreover, the system must be equipped with mechanical pumps, which leads to higher fabrication costs and heating effects due to friction. Alternatively, a material can also be moved with externally applied electrical fields, which is referred to as electrokinetic phenomena (Canpolat et al., 2013b). In these systems, electrodes are embedded in the channel to implement electrical fields to the flow domain; thus, the drawbacks of pressure-driven systems are avoided. By this way, the parabolic flow profile is replaced with a plug-like flow profile. These flow systems allow to control fluid and particles by miniaturizing the geometry of the design, which is one of the advantages of microfluidic applications. For instance, a few circulating tumor cells are isolated from the whole blood in the work of Sarioglu et al. (2015), optimum sizes of the liposomes are investigated to the extent of drug delivery vehicles in the work of Andar et al. (2014), an efficient gene delivery is carried out to hard-to-transfect typed cells by Hur et al. (2020), and some biological toxins as far as to picomolar levels are able to be detected by Meagher et al. (2008). Moreover, several additional precious advantages can be attributed to microfluidic systems, which can be sorted as improved control on the fluid flow, low sample consumption, low analysis duration, high sensitivity, portability, and readily integration with useful parts. Fluids are also mobilized with surface acoustic waves (SAW) in many studies, such as analysis of water droplet motion for varying RF powers and frequencies (Insepov et al., 2021), investigation of SAW control parameters on the sessile drop under gravitational force (Noori et al., 2021), analyzing acoustophoretic movement of polystyrene beads, white blood cells, MCF-7 breast cancer cells (Namnabat et al., 2021), generation of heating in a fluid (Das et al., 2019). Generally, applications of microfluidics, especially in the bioscience are conducted under low Reynolds number (Re), Re<<1 (Tatlısoz and Canpolat, 2018). Because effective control of synthetic and biological particles can be achieved, and high shear stresses due to the high Re number can also threaten the conservation of the structure and function of biological molecules such as enzymes, proteins, and cells. For instance, the intracellular transport of biomolecules under electroosmotic flow conditions is modeled by Andreev approximately at $Re \approx 10^{-5}$, droplets are formed with $Re = 1.16 \times 10^{-7}$ in the work of Fadhil Majnis et al. (2018), micromixing with the magnetically actuated cilia is carried out at $Re = 1.16 \times 10^{-3}$ by Wu et al. (2017), uneven colloidal particles are transported in coordinate for $Re < 10^{-4}$ according to the work of Reinmüller et al. (2013), simulating circulating tumor cell movement in an arteriole is performed under $Re = 2.98 \times 10^{-3}$ as proposed in the work of Xiao et al. (2021). Moreover, transport in a nanopore with electroosmotic or pressure-driven flow occurs in a low Reynolds number regime (Mao et al., 2014).

Machine learning is an extremely popular topic among scientific studies, due to its feasibility in many diverse areas, such as energy management (Musbah et al., 2021), chemical reactions (Singh et al., 2019), two-phase flows (Jalili et al., 2024), etc. Neural networks are a subset of machine learning that utilizes densely interconnected neurons to solve problems. Training of the neural network is possible solely with the datasets. However, this approach is impractical for many problems, due to the demand for large datasets and being deprived of physical constraints. Raissi et al. (2019) developed PINN to address this issue. Either forward or inverse problems are described as partial differential equations (PDEs) and solved with neural networks. Moreover, physical constraints can be incorporated into the model with PINN; thus, the accuracy of the results can be enhanced. Navier-Stokes Equation is frequently introduced to PINN for various flow problems, such as aneurysms in blood vessels (Oldenburg et al., 2023), the flows with vortex-induced vibrations (Bai and Zhang, 2022), and the investigation of fluid flow around circular and elliptical solid particles (Hu and McDaniel, 2023). PINN is also considered to solve the transport problems of the materials via the Nernst-Planck Equation (Huang et al., 2024). However, many problems should be described with both the Navier-Stokes Equation and the Nernst-Planck Equation, such as electrokinetic fluid flow through a nanopore (Mao et al., 2014), investigating flow effects on ion-selective electrodes (Andrews et al., 2023), directing and capturing of the DNA particle in a nanopore (Paik et al., 2012), electrodiffusion in fluids (Constantin et al., 2021), ion transport throughout a porous medium (Agnaou et al., 2020).

In this study, Navier-Stokes and Nernst-Planck equations are solved simultaneously with PINN to understand the liquid flow and species transport along a straight microchannel under pressure-driven and electroosmotic flow conditions for various Reynolds numbers within $5 \times 10^{-6} \leq Re \leq 5 \times 10^{-2}$. When the time-independent problem calculations are completed, time-dependent versions of the given problems are introduced to the PINN. In this sense, liquid flow is generated by a pressure difference or electrokinetically. The same models are established with the finite element solver COMSOL Multiphysics, and the obtained results from the PINN are validated through comparison. The PDEs are solved with neurons and weight parameters by PINN. Acquiring matching results with different solving techniques can be submitted as a powerful verification method.

1.1 Novelty of the study

The present investigation provides a novel approach utilizing the Physics-Informed Neural Network (PINN) for modeling the fluid and species transport along a microchannel, which is the critical

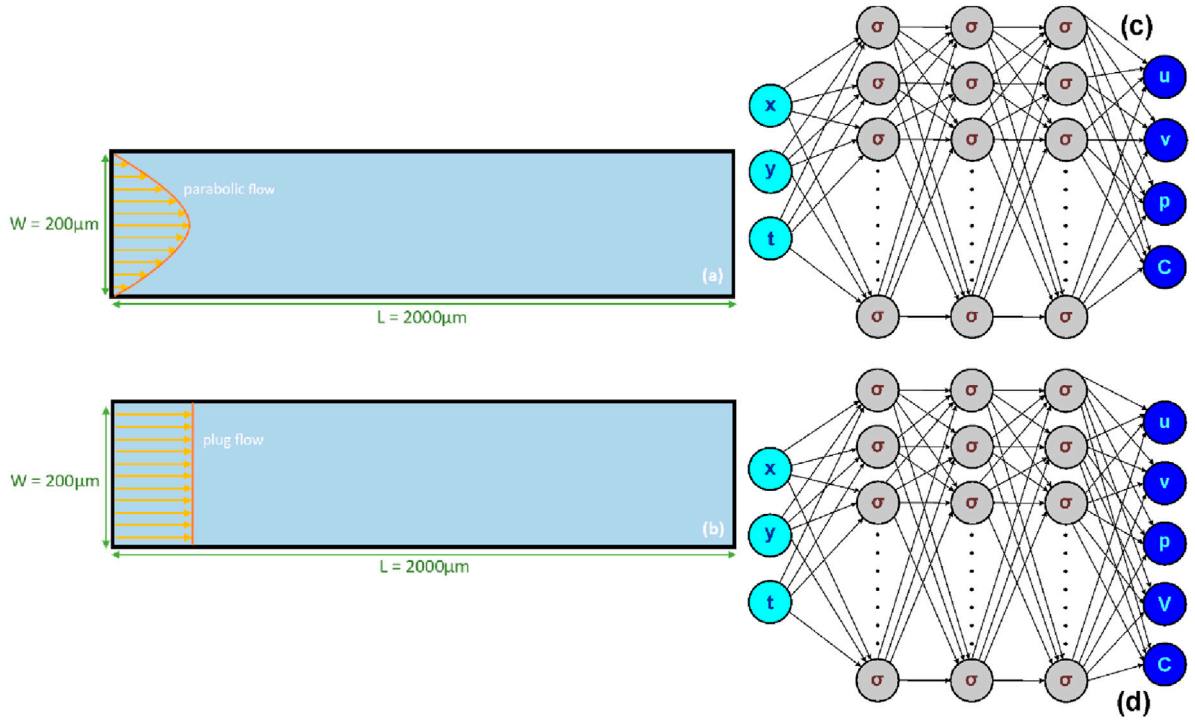

FIGURE 1
(a) Parabolic flow profile is governed in a microchannel with the length of L = 200 μm and width of W = 20 μm **(b)** Plug-like flow profile is governed in a microchannel with the length of L = 200 μm and width of W = 20 μm **(c)** Designed neural network to solve pressure-difference problems **(d)** Designed neural network to solve electrokinetically-driven problems.

component for bio-/microfluidic devices. These transport mechanisms are analyzed under pressure gradients and electrokinetic forces, which are the primary driving mechanisms in microfluidics. For this purpose, the Navier-Stokes and the Nernst-Planck equations are coupled on the common term velocity. In contrast to the previous studies, this work introduces a key refinement by defining the pressure scale based on the inlet pressure value; thus, lower error margins are achieved during the neural network training. The calculated results of the PINN are compared with the Finite Element Analysis (FEA) software COMSOL Multiphysics, whose results are highly consistent with the actual results. Thus, outcomes of the PINN can be evaluated using actual values. This proposed model can be safely implemented in biomedical engineering designs, including mass transport, bioreactors, bioanalytical devices, micromixers, etc. Given the growing interest in PINN-based solutions recently, PINN has been an emerging field and has gathered significant attention. We believe this work will attract considerable interest within the relevant community and contribute to ongoing achievements in the field.

2 Materials and methods

The fluid flow is modeled in a 2-dimensional (2D) rectangular channel, which has a length of L = 200 μm and width of W = 20 μm, as shown for parabolic flow and plug-like flow profiles in Figures 1a,b, respectively. Left and right boundaries of the microchannel are determined as the inlet and the outlet, respectively. The fluid is characterized as Newtonian and incompressible, while its flow behavior is described with time-dependent Navier-Stokes equations along with the continuity equation, as shown below:

$$\rho \frac{\partial \boldsymbol{u}}{\partial t} = -\nabla p + \mu \nabla^2 \boldsymbol{V} + \boldsymbol{f} \tag{1}$$

$$\nabla . \boldsymbol{V} = 0 \tag{2}$$

where the symbols of **V**, ρ, p, μ, **f** (Equations 1, 2) are velocity, density, viscosity, pressure, and body force, respectively. The bold characters are preferred to indicate vector quantities. The inertial term is excluded from Equation 1, due to the very low Re being effective, such as Re = 5×10^{-6}, 5×10^{-4}, and 5×10^{-2} (Ai et al., 2009; Namnabat et al., 2021). Under these circumstances, flow disturbances on the biological specimen can be avoided, and more functionality can be gained from shorter microfluidic channels with enhanced control of whole microfluidic system. Moreover, the body force term equals zero, due to no external body force acting on the system for all developed models. All the parameter values are listed in Table 1.

Fluid flow is generated either pressure-driven or electrokinetically. For pressure-driven flow, a pressure gradient is established throughout the channel, by applying an equation for parabolic velocity profile to the inlet of the microchannel, as shown in Equation 3:

$$\boldsymbol{u}_{\boldsymbol{parabolic}} = \frac{\Delta p W^2}{8 \mu L} \left(1 - \frac{4 y^2}{W^2} \right) \tag{3}$$

where Δp is the pressure drop through the channel length, which equals to difference between inlet and outlet pressures, i.e., P_{in}–P_{out}. Moreover, outlet pressure is defined as zero, and zero velocity is

TABLE 1 Parameters and definitions used in the present study.

Symbol	Definition	Value
W	Width of the channel	20 μm
L	Length of the channel	200 μm
μ	Viscosity of the fluid	10^{-3} Pa. s
ρ	Density of the fluid	1,000 kg/m^3
p_{in}	Inlet pressure	10^{-3} Pa
ε_0	Permittivity of free space	8.854×10^{-12} F/m
ε_r	Relative permittivity of the fluid	80
ζ	Zeta potential of the channel walls	−0.01 V
ϕ_{in}	Inlet potential	0.0070621 V
D	Diffusion coefficient of the diluted species	10^{-10} m^2/s
C_{in}	Inlet concentration	5 mol/m^3
D_{scale}	Diffusion coefficient term scaling factor	10^{-10} m^2/s
P_{scale}	Pressure term scaling factor	10^{-3} Pa
C_{scale}	Concentration term scaling factor	5 mol/m^3
ϕ_{scale}	Electric potential term scaling factor	0.0070621 V
u_{scale}	Velocity term scaling factor	2.5×10^{-7} m/s
L*	Dimensionless length of the channel	1 (=L/L)
W*	Dimensionless width of the channel	0.1 (=W/L)
D*	Dimensionless diffusion coefficient of the diluted species	1 (=D/D_{scale})
P*	Dimensionless inlet pressure	1 (=P/P_{scale})
C*	Dimensionless inlet concentration	1 (=C_{in}/C_{scale})
φ*	Dimensionless inlet potential	1 (=φ_{in}/φ_{scale})

defined to the upper and lower walls of the microchannel due to no-slip boundary condition. If the electroosmotic flow is in question, a potential is defined to the inlet of the channel, ϕ_{in}, and the outlet is grounded. Therefore, an electrical potential gradient is established throughout the channel. With the assigned anode potential, flow velocity through the cross-section of the channel equals the maximum velocity value for the pressure-driven flow. Because the channel width is scaled to the extent of micrometers, the existence of an electrical double layer (EDL), in the vicinity of the upper and lower boundaries is neglected. The characteristic nano-scaled thickness of EDL is much lower than the proposed micro-scaled channel width; hence, this approximation is valid (de Rutte et al., 2016). Therefore, Smoluchowski slip velocity is applied to both upper and lower boundaries of the microchannel, instead of the no-slip boundary condition, as given in Equation 4:

$$\boldsymbol{u}_{eo_w} = -\frac{\varepsilon\zeta_w}{\mu}\boldsymbol{E}_t \tag{4}$$

where the symbols of ε, ζ_w, μ, $\mathbf{E_t}$ are the electrical permittivity, zeta potential of the microchannel walls, the viscosity, and the tangential component of the external electrical field. Due to 2D design in Cartesian coordinates, vectorial quantities are comprised of x- and y-components. Therefore, the x-component and y-component of the velocity quantity are denoted as **u** and **v**, respectively. While non-zero velocity values are always attributed to the **u** component, a zero value is always defined for the **v** component. Another outcome of the no-EDL approximation is related to the electrical charge distribution within the microchannel. Laplace equation, Equation 5, is employed for solution domain, instead of the Poisson equation, due to the elimination of the only net charge, including the area within the cross-section of the channel:

$$\nabla^2\phi = 0 \tag{5}$$

where ϕ is the electrical potential.

A single chemical species is dissolved within the fluid. Transport of the dissolved species is described with Equation 6, which is time-dependent Nernst-Planck Equation:

$$\frac{\partial C}{\partial t} = D\nabla^2 C - \boldsymbol{V}.\nabla C \tag{6}$$

where the symbols of C and D are the concentration and diffusion coefficient of the diluted species, respectively. While first term of the right side of the equation is the diffusive flux, and the second term is the convective flux. The diffusion coefficient is assumed constant,

due to the usage of a single type of fluid, isothermal conditions, and low pressure drop between the inlet and the outlet. Accordingly, term **V** is assigned as the coupling parameters, due to the co-existence of the Navier-Stokes and the Nernst-Planck equations. Note that the chemical species is assumed as neutral; thus, the electromigration term of the Nernst-Planck equation is discarded. If the isoelectric point of the relevant species is equalized to the ambient pH, zero electromigration can be obtained. The entrance of the chemical species to the microchannel is carried out by defining a constant concentration at the inlet, $C = C_{in}$. The chemical species is collected from the outlet. The upper and lower boundaries are defined as non-permeable, as well. These definitions are implemented to the system by Equation 7:

$$\boldsymbol{n}.D\nabla C = 0 \tag{7}$$

The proposed models are carried out with PINN as well as commercial simulation software COMSOL Multiphysics, and subsequently the acquired solutions are compared. Because FEA is utilized by COMSOL Multiphysics for problem-solving, a mesh with tetragonal elements is applied to the microchannel domain. A model is consecutively solved for meshes with 1,000–2000–3,000–4,000–16000 quadrangle elements, and less than 1% solving difference is observed between the last two combinations. Therefore, the mesh with 4,000 elements is used for all FEA models. Instead of discretization by meshing, governing equations and boundary/initial conditions are converted to an optimization problem, whose performance is qualitatively evaluated by a loss function, for PINN modeling. Estimations are made in an unsupervised manner according to some specific points within the space-time domain to minimize the loss function. Therefore, the proposed mathematical model is introduced to a neural network with three hidden layers of 100 neurons. The neuron number of the outlet layer always equals to the number of dependent variables, such as x-velocity, y-velocity, pressure, and concentration for the current problem. For the model including the electrokinetics phenomenon, the electrical potential difference is incorporated into the model; hence, five neurons are located in the output layer. Correspondingly, neuron numbers of the inlet are determined according to the number of independent variables of the problem, which are the x-coordinate, the y-coordinate, and time. Therefore, three and two neurons are stationed at the inlet boundary for time-dependent and steady problems, respectively. Weight parameters are defined upon all these connections and loss function is diminished by solely altering the weight parameters during the problem solving. Hyperbolic tangent function (tanh) is applied inside of the neurons as an activation function (σ), due to better approximation performance on the analytical function (De Ryck et al., 2021). Adam optimizer is used for training the neural network, which is based on gradient descent algorithm with adaptive learning rates for weight parameters (Kingma and Ba, 2014). After 40,000 iterations with the learning rate of 1×10^{-4}, L-BFGS optimizer is employed to further reduce the loss function. L-BFGS is the memory efficient version of a quasi-Newton algorithm BFGS, which uses line search to determine the optimum weight parameters (Rafati and Marica, 2020). The simulations are sustained for t = 200 s, due to system can substantially approach to steady-state within this duration. The PINN model is designed by benefiting from the DeepXDE library, which was developed by Lu et al. (2021) in the Python programming language.

The neural networks for the pressure-driven and the electrokinetically-driven systems are schematized in Figures 1c,d, respectively.

Initially, the problems are defined as time-independent; hence, the time neuron is subtracted from the inlet layer and the term in the left-hand side of the equation is discarded. Moreover, the governing equations and boundary conditions are nondimensionalized for better training of the model. Some scaling parameters are defined for the variables of the aforementioned equations with the purpose of nondimensionalization. L, p_{in}, D, C_{in} is used as length scale, pressure scale, diffusion coefficient scale, and concentration scale, respectively. Accordingly, the maximum value of the parabolic velocity profile is used as the velocity scale, which equals $u_{scale} = (\Delta p W^2)/(8\ \mu L)$, and the time scale is determined as $t_{scale} = L/u_{scale}$. Sincethe pressure scale is assigned as $p_{scale} = \mu u_{scale}/L$, in accordance with the usual approach, the error margins can solely be diminished to 1.03×10^{-1} and 1.23×10^{-1} for steady and time-dependent pressure-driven problems. Therefore, the obtained solutions are diverted from the exact values. On the contrary, 3.04×10^{-5} and 4.76×10^{-3} error margins are reached for steady and time-dependent problems, respectively, when $p_{scale} = p_{in}$. During the solving of steady problems, time-dependent parameters at the left-hand side of the Navier-Stokes and the Nernst-Planck equations are omitted. For PINN solving, time-dependent parameter of the Navier-Stokes Equation is not considered for the purpose of alleviating the computational burden. On the other hand, no pressure difference is exerted on the electrokinetically-driven system; hence, p_{in} is defined as unity to prevent the production of infinitive value in the Navier-Stokes Equation. As a result, all governing equations, such as the Navier-Stokes equation, continuity equation, Nernst- Planck equation, and Laplace equation, are nondimensionalized as given in Equations 8–11, respectively:

$$0 = -\nabla^* p^* + \left(\frac{\mu u_{scale}}{p_{scale} L}\right)\nabla^{*2}\boldsymbol{V}^* \tag{8}$$

$$\nabla^*.\boldsymbol{V}^* = 0 \tag{9}$$

$$\frac{\partial C^*}{\partial t} = \frac{1}{Pe}D^*\nabla^{*2}C^* - (\boldsymbol{u}^*.\nabla^* C^*) \tag{10}$$

$$\nabla^{*2}\phi^* = 0 \tag{11}$$

where Pe is the dimensionless Peclet number describing the ratio between the convective and diffusive fluxes, as $Pe = (u_{scale}L)/D$. The input variables and boundary/initial conditions are nondimensionalized, as well, which are shown in Equations 12–27:

$$x^* = \frac{x}{L} \tag{12}$$

$$y^* = \frac{y}{L} \tag{13}$$

$$t^* = \frac{t}{t_{scale}} \tag{14}$$

$$P_{in}^{*} = 1\ if\ x^{*} = 0\ and\ y^{*} = [0, 0.1]\ \text{for pressure – driven flow conditions} \quad (15)$$

$$P_{in}^{*} = 0\ if\ x^{*} = 1\ and\ y^{*} = [0, 0.1]\ \text{for pressure – driven flow conditions} \quad (16)$$

$$P_{in}^{*} = 0\ if\ x^{*} = 0\ and\ y^{*} = [0, 0.1]\ \text{for electroosmotic flow conditions} \quad (17)$$

$$P_{in}^{*} = 0\ if\ x^{*} = 1\ and\ y^{*} = [0, 0.1]\ \text{for electroosmotic flow conditions} \quad (18)$$

$$V_{in}^{*} = \frac{V_{in}}{V_{scale}}\ if\ x^{*} = 0\ and\ y^{*} = [0, 0.1] \quad (19)$$

$$\boldsymbol{u}^{*} = \left(1 - \frac{4y^{*2}}{W^{*2}}\right) if\ x^{*} = 0\ and\ y^{*} = [0, 0.1] \quad (20)$$

$$\boldsymbol{u}_{\boldsymbol{p}}^{*} = 0\ if\ x^{*} = [0, 1]\ and\ y^{*} = 0\ or\ 1 \quad (21)$$

$$\boldsymbol{u}_{\boldsymbol{eo_w}}^{*} = 1\ if\ x^{*} = [0, 1]\ and\ y^{*} = 0\ or\ 1 \quad (22)$$

$$\boldsymbol{v}^{*} = 0\ for\ all\ boundaries \quad (23)$$

$$C_{in}^{*} = \frac{C_{in}}{C_{scale}}\ if\ x^{*} = 0\ and\ y^{*} = [0, 0.1] \quad (24)$$

$$\frac{\partial C^{*}}{\partial x^{*}} = 0\ if\ x^{*} = 0\ or\ 1\ and\ y^{*} = [0, 0.1] \quad (25)$$

$$\frac{\partial C^{*}}{\partial y^{*}} = 0\ if\ x^{*} = [0, 1]\ and\ y^{*} = 0\ or\ 1 \quad (26)$$

$$C^{*} = 0\ if\ t^{*} = 0 \quad (27)$$

Training and test performances of the PINN are evaluated by calculating the loss value to the mean-squared error (MSE) approach for each of the partial differential equations and the boundary/ initial condition, as given in Equation 28:

$$\mathcal{L} = MSE_f + MSE_b + MSE_{init} \quad (28)$$

where $\mathcal{L}$ is the total loss value. MSE_f, MSE_b, MSE_{init} are mean-squared errors of the partial differential equations, boundary conditions, and the initial conditions, respectively, and calculated as shown in Equations 29–31, respectively:

$$MSE_f = \frac{1}{N}\sum_{i=1}^{N}\left|f\left(t^{*i}_f, x^{*i}_f, y^{*i}_f\right)\right|^2 \quad (29)$$

$$MSE_b = \frac{1}{N}\sum_{i=1}^{N}\left|\tilde{u}\left(t^{*i}_f, x^{*i}_f, y^{*i}_f\right) - \tilde{u}^{i}\right|^2 \quad (30)$$

$$MSE_{init} = \frac{1}{N}\sum_{i=1}^{N}\left|\bar{\bar{u}}\left(t^{*i}_f, x^{*i}_f, y^{*i}_f\right) - \bar{u}^{i}\right|^2 \quad (31)$$

while $f(t^{*i}_f, x^{*i}_f, y^{*i}_f)$, $\tilde{u}(t^{*i}_f, x^{*i}_f, y^{*i}_f)$, $\bar{\bar{u}}(t^{*i}_f, x^{*i}_f, y^{*i}_f)$ are the calculated values from the partial differential equation, boundary condition, initial condition at the relevant collocation points and the given time, respectively; the symbols ũ, ū represent the exact boundary condition value and the exact initial condition value, respectively.

3 Results and discussion

Before solving the actual problems with PINN, it is necessary to determine the optimal number of hidden layers and the number of neurons per hidden layer, followed by optimizing the number of domain points (Nd) and the number of boundary/initial points (Nb,i). By this means, the steady electrokinetic model is solved for 20,000 iterations according to a combination of the number of neurons and the number of hidden layers. The hidden layers of 2-3-4 are consecutively tested with 50–100–150 neurons per hidden layer, as shown in Table 2. The optimal layer and neuron numbers are determined as 3 and 100, respectively, based on the lowest error margin. Afterwards, a series of domain points and boundary points are introduced to the optimum neural network. The collation points of 500–1,000–2000–3,000–5,000 are defined in the computation domain along with 500/500–1,000/1,000–2000/2000–3,000/3,000 boundary points/initial points, successively. As seen in Table 3, the lowest error margin is recorded for 3,000 domain points and 3,000/3,000 boundary/initial points. Moreover, no significant overfitting is observed with the given hyperparameters. The analyses are carried out in a workstation, which has an Intel Xeon 2.40 GHz CPU and 64 GB RAM, after approximately 25 h, with memory usage of approximately 3500 MB. However, the problem-solving is completed in a few minutes and approximately 1500 MB of memory usage with COMSOL Multiphysics. It can be concluded that artificial neural networks requires more improvements to lower the necessary duration and memory for problem-solving compared to finite element method. For this purpose, one of the suggestion is dividing the excess analysis data by the decentralization method to diminish the duration for PINN (Yang et al., 2025).

TABLE 2 Error margins for varied hidden layer numbers against varied neuron numbers.

Neurons layers	50	100	200
2	2.57E-02	2.93E-02	1.89E-02
3	2.11E-02	4.29E-04	2.63E-02
4	1.05E-02	1.31E-02	1.51E-02

TABLE 3 Error margins for varied boundary/initial point numbers against varied domain points.

$N_{b,i}$ / N_d	500	1,000	2,000	3,000	5,000
500–500	1.35E-02	2.21E-02	8.08E-03	9.27E-03	1.02E-02
1,000–1,000	1.08E-02	8.60E-03	1.33E-02	9.78E-03	7.47E-03
2,000–2,000	1.59E-02	1.02E-02	2.31E-02	7.02E-02	1.74E-02
3,000–3,000	1.37E-02	1.33E-02	1.10E-02	4.29E-04	1.52E-02

Due to outcomes of FEA are utilized to evaluate the accuracy of the PINN solutions, COMSOL Multiphysics calculations are validated by using the results of Yuan et al. (2023), and significantly overlapping results are obtained, as shown Supplementary Figure S1. As the initial problem, a steady pressure-driven system is considered. In Figure 2, dependent parameters of x-velocity, y-velocity, pressure, and concentration are visualized according to the calculations of PINN with 3.04×10^{-5} error margin. A parabolic flow profile is observed for x-velocity, as can be seen in Figure 2a. That is, the minimum velocity magnitudes

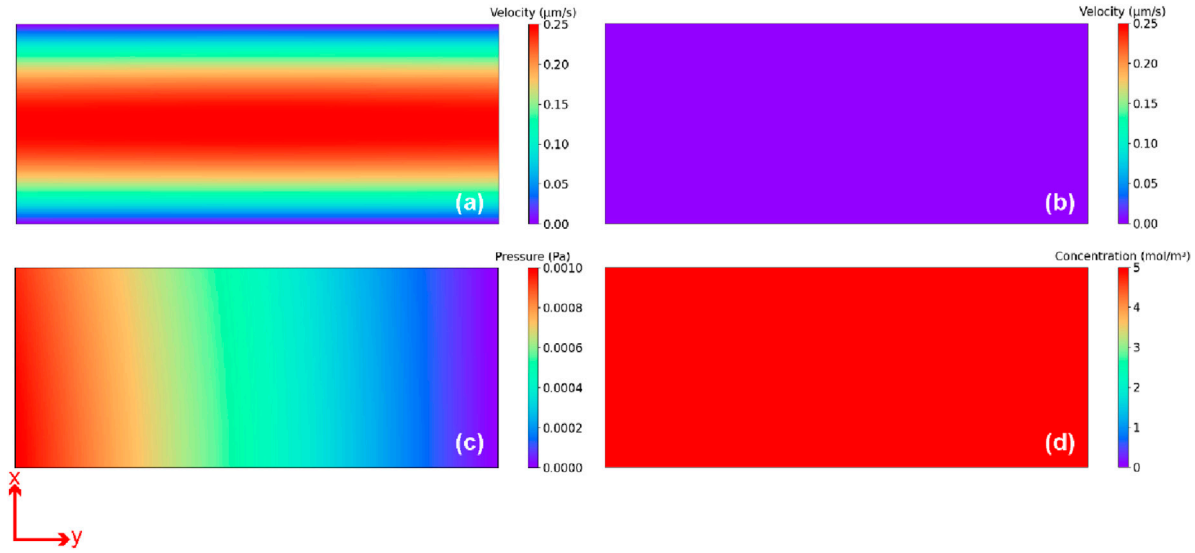

FIGURE 2
(a) The distribution of streamwise velocity magnitude under pressure-driven flow conditions, **(b)** The distribution of transverse velocity magnitude under pressure-driven flow conditions, **(c)** The distribution of pressure magnitude under pressure-driven flow conditions, **(d)** The distribution of chemical species at rest in the solution domain for pressure-driven flow conditions.

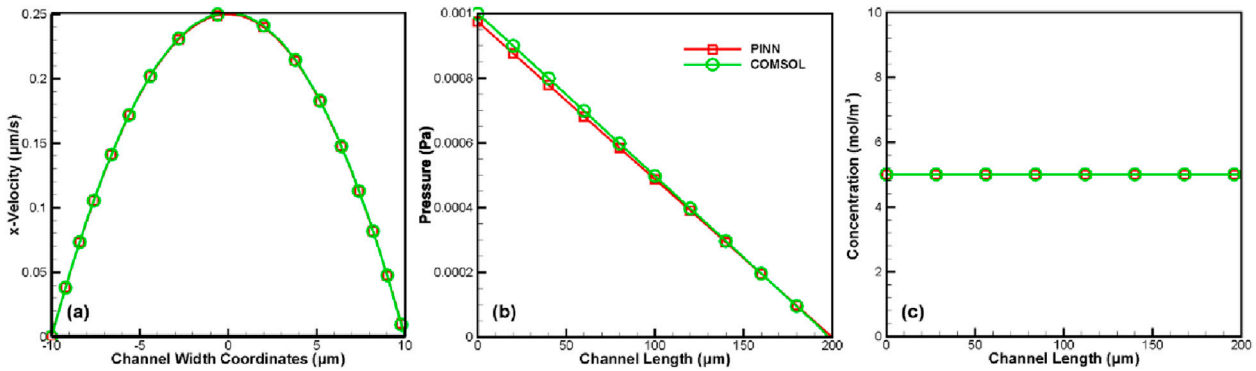

FIGURE 3
(a) The plot of streamwise velocity magnitude obtained from PINN and FEA analysis, **(b)** The plot of pressure variation along the centerline of the microchannelsd according to both PINN and COMSOL Multiphysics **(c)** Uniform concentration profile is observed throughout the length of the microchannel for PINN and COMSOL Multiphysics.

are calculated in the vicinity of upper and lower boundaries and the maximum velocity magnitude is obtained on the centerline of the microchannel. While the x-velocity at the boundaries is calculated as zero due to no-slip boundary condition, the maximum velocity magnitude along the centerline is calculated as $\mathbf{u}$ = 0.25 μm/s. On the other hand, no velocity magnitude for y-component is obtained for all points within the computational domain, as seen in Figure 2b. The pressure magnitude starts from p_{in} = 0.001 Pa and decreases linearly to zero from the inlet to the outlet, as depicted in Figure 2c. Chemical species are uniformly scattered throughout the microchannel with the prescribed feeding value at the inlet, C_0 = 5 mol/m^{3,} as shown in Figure 2d.

The calculations of the PINN are compared with those from COMSOL Multiphysics, and the results are graphically exhibited in Figure 3. The values of x-velocity are plotted *versus* the cross-section of the microchannel, and the results from two different solvers are strongly consistent, as seen in Figure 3a. Although the graphical data is not shown here, zero y-velocity values are also observed on every point for COMSOL Multiphysics. In contrast to the variable of x-velocity, pressure, and concentration variables are graphitized through the longitudinal section of the microchannel. As seen in Figures 3b,c, the outcomes of pressure and concentration from PINN and COMSOL Multiphysics are evaluated as highly consistent, respectively. While the ultimate goal is to predict concentration distribution within the computational domain, root mean square error (RMSE) is calculated for the concentration profiles, which is 0.001 for steady pressure-driven flow.

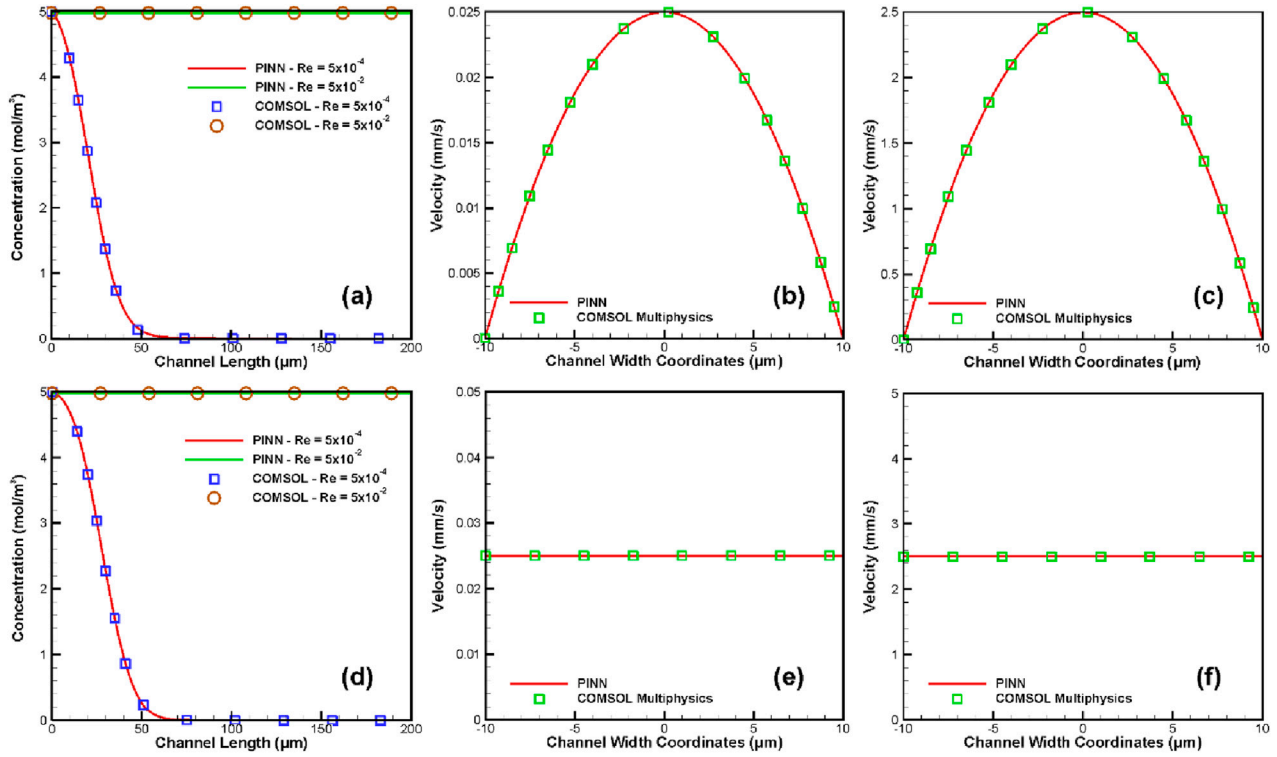

FIGURE 4
(a) Concentration profiles of the pressure-driven flow along the centerline of the microchannel for both Re = 5×10^{-4} and Re = 5×10^{-2} **(b)** Velocity profile of the pressure-driven flow from lower wall to upper wall for Re = 5×10^{-4} **(c)** Velocity profile of the pressure-driven flow from lower wall to upper wall for Re = 5×10^{-2} **(d)** Concentration profiles of the electroosmotic flow along the centerline of the microchannel for both Re = 5×10^{-4} and Re = 5×10^{-2} **(e)** Velocity profile of the electroosmotic flow from lower wall to upper wall for Re = 5×10^{-4} **(f)** Velocity profile of the electroosmotic flow from lower wall to upper wall for Re = 5×10^{-2}.

To present the prediction performance of the PINN for higher Reynolds numbers, the velocity and concentration profiles at Re = 5×10^{-4} and Re = 5×10^{-2} are conducted. The Re number is raised to Re = 5×10^{-4} and Re = 5×10^{-2} by increasing the velocity magnitude of the flow, and the results are plotted in Figure 4. Note that, the first row demonstrates the results of pressure-driven flow and the second row presents those of electroosmotic flow. The concentration distributions at Re = 5×10^{-4} and Re = 5×10^{-2} along the centerline of the microchannel within 1s are shown in Figures 4a,d, respectively. At Re = 5×10^{-4}, the concentration can only reach approximately 60 μm from the channel wall in the streamwise direction within 1s. However, the concentration can reach the exit wall of the channel within 1s at Re = 5×10^{-2}. In both results, PINN and COMSOL data are in good agreement. The velocity profiles of PINN at both Reynolds numbers for pressure-driven and electroosmotic flows exhibit excellent compatibility with those obtained from COMSOL Multiphysics, as seen in Figures 4b,c,e,f. The maximum x-velocity values are u = 0.025 mm/s and u = 2.5 mm/s for Re = 5×10^{-4} and Re = 5×10^{-2}, respectively.

Fluid flow in the previous steady model is driven electrokinetically via PINN with 3.60×10^{-4} error margin. As seen in Figure 5a, x-velocity is uniform throughout the entire domain; hence, plug-like flow profile is obtained. Uniformly divided zero magnitude is also observed for y-velocity, as illustrated in Figure 5b. As depicted in Figure 5c, the electrical potential is linearly decreased from the maximum value of ϕ = 0.0070621 V to zero from the inlet to the outlet. Chemical species are uniformly filled to the microchannel domain with the determined inlet concentration of C_0 = 5 mol/m³, as shown in Figure 5d.

Numerical values from the given dependent variables are schematized in Figure 6. As shown in Figure 6a, the x-velocity along the width of the microchannel remains constant, which overlaps exactly with the outcome of COMSOL Multiphysics. The value of the fluid velocity along the x-direction is calculated as $\mathbf{u}$ = 0.25 μm, equal to the maximum value of the pressure-driven flow. Similar to PINN, FEA solution results in no variation in y-velocity magnitude. Besides, electrical potential solving along the length of the microchannel is nearly identical between PINN and FEA, as shown in Figure 6b. Overlapping the outcomes of two solvers is also obtained for concentration values, which are plotted along the microchannel length in Figure 6c while RMSE = 0.003.

The transport of the species is solved in a time-dependent domain, while the other parameters are kept the same. In contrast with PINN solver, time-dependent velocity term is included to Navier-Stokes equation for finite element solver. Nevertheless, x-velocity, y-velocity and pressure profiles are perfectly matched for pressure-driven, and electroosmotic flows, where x-velocity profiles are presented in Figures 7a,b. Therefore,

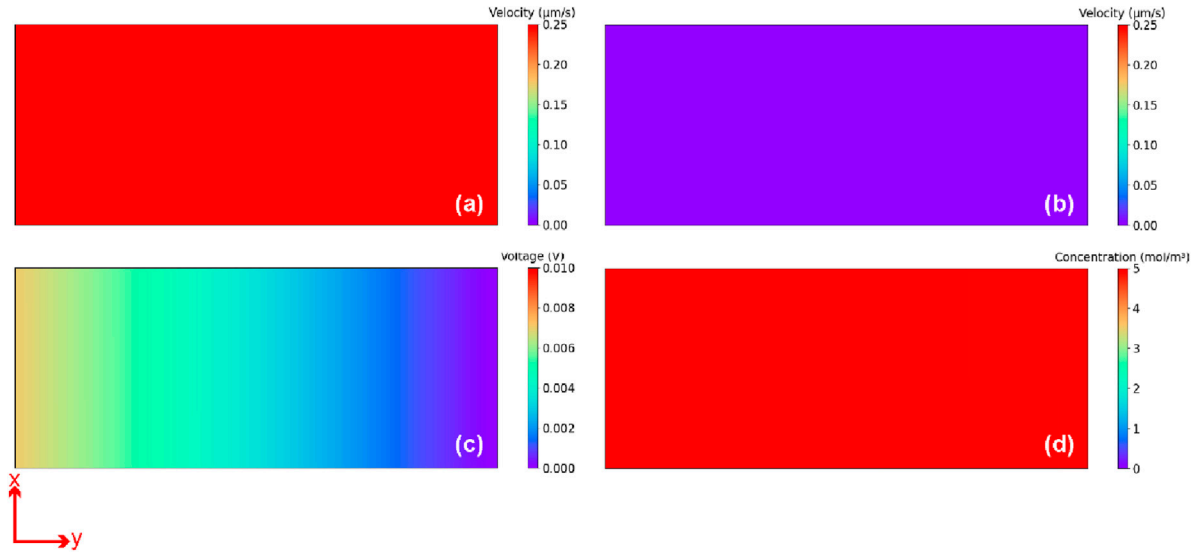

FIGURE 5
(a) The distribution of x-velocity in the microchannel domain **(b)** The distribution of y-velocity in the microchannel domain **(c)** The variation of electrical potential from the inlet to the outlet **(d)** The distribution of chemical species in the microchannel.

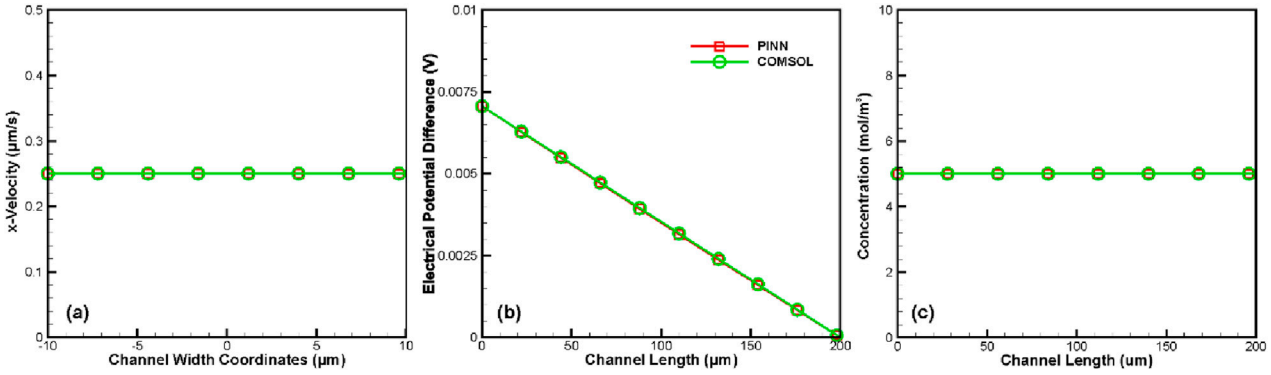

FIGURE 6
(a) x-velocity magnitudes of electroosmotic flow for PINN and FEA solutions, **(b)** Electric potential values obtained from PINN and FEA solutions, **(c)** concentration profiles obtained from PINN and FEA solutions.

computational cost is decreased in PINN solution using this strategy safely. On the other hand, the time-dependent concentration term is included in the Nernst-Planck Equation for both solvers. Therefore, the distribution of the chemical species is altered as time progresses. Concentration maps of PINN calculations are illustrated in Figure 8, whose error margin is 4.76×10^{-3}. As seen in Figure 8a, half of the maximum concentration value is reached at approximately 75 μm length of the channel at t = 50 s. Besides, half maximum concentration value is observed for t = 100 s at approximately 120 μm length, as shown in Figure 8b. Chemical species are further pushed through the channel length, and half of the maximum concentration value is barely observed adjacent to the outlet for t = 150 s, as shown in Figure 8c. Following the general trend, half of the maximum value is exceeded at every point for the last second, as shown in Figure 8d. Though the lowest value is calculated at the outlet, higher than C = 3 mol/m^3 is effective.

Concentration values from the previous maps are also schematically displayed in Figure 9. Curves are plotted along the centerline of the microchannel with both PINN and FEA. A good agreement is observed among the solutions of the solvers. Concentration values are initialized from the prescribed inlet concentration, which is C_0 = 5 mol/m^3, and decreased quadratically towards the outlet. According to PINN, the chemical species is accumulated on the outlet as corresponding to C = 0.52 mol/m^3 at t = 50 s, this value is gradually increased to C = 1.75 mol/m^3, C = 2.71 mol/m^3, C = 3.36 mol/m^3 for t = 100s-150s–200 s, respectively. From the perspective of FEA, these values are calculated as C = 0.52 mol/m^3, C = 1.75 mol/m^3,

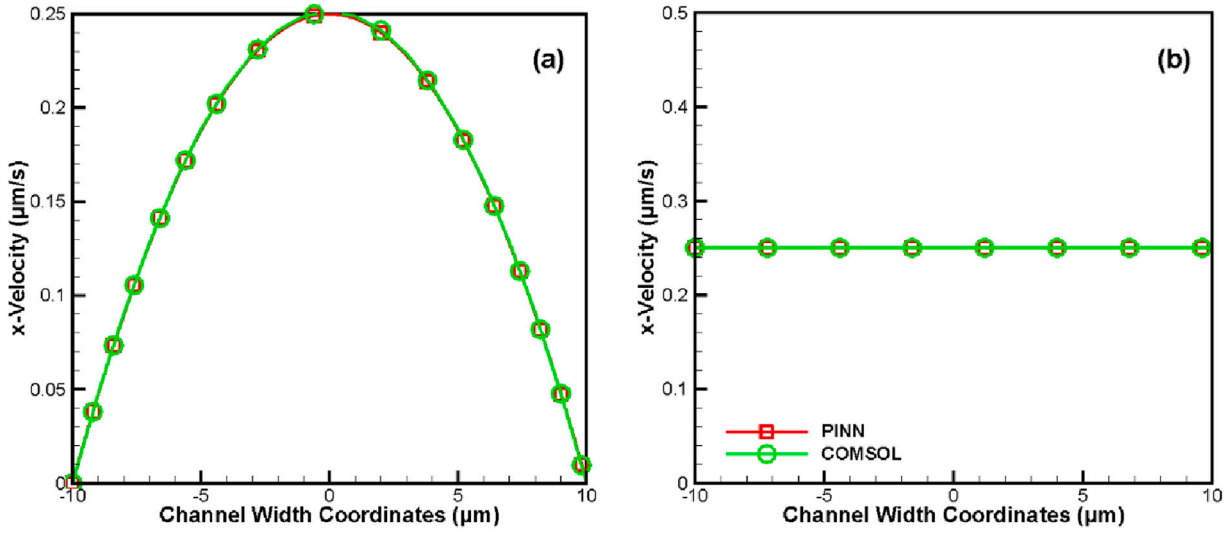

FIGURE 7
Comparison of x-velocity profiles of steady PINN solutions and time-dependent COMSOL Multiphysics for **(a)** pressure-driven flow and **(b)** electrokinetically-driven flow.

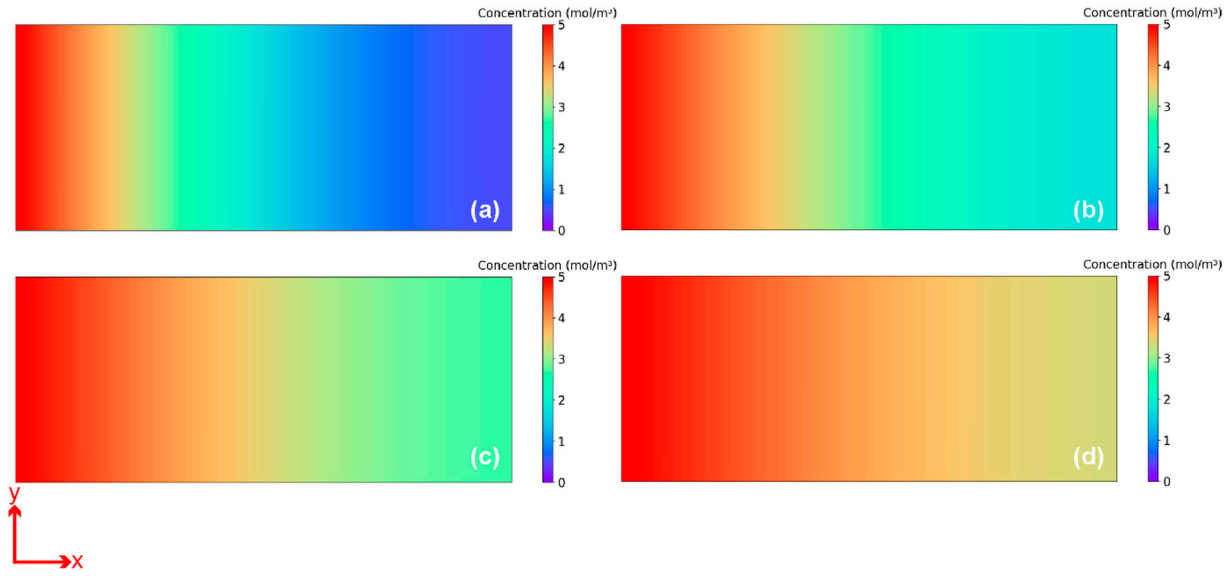

FIGURE 8
Chemical species transport under pressure-driven flow conditions for the moments of **(a)** t = 50 s **(b)** t = 100 s **(c)** t = 150 s **(d)** 200 s.

C = 2.71 mol/m^3, C = 3.39 mol/m^3 for t = 50–100-150–200 s, respectively. For each of the given time steps RMSE values are calculated, such as 0.033–0.005–0.006–0.025 in ascending order.

Electrokinetically-driven system is adapted to a time-dependent problem via PINN, with 6.02×10^{-3} error margin. The Navier-Stokes and the Continuity equations remain steady-state, similar to the pressure-driven modeling. Moreover, no time-dependent component is intrinsically possessed by the Laplace Equation. Therefore, transformation to time-dependent formation is solely implemented in the Nernst-Planck Equation. As a result, identical calculations are carried out for all dependent variables, except for the concentration. Concentration maps are derived from PINN and depicted for t = 50–100-150–200 s in Figures 10a–d, respectively. Chemical species are moved from the inlet to the outlet, which leads to a filled microchannel with prescribed inlet concentration.

Concentration values are specified along with FEA in Figure 11, which are plotted as a quadratically decreasing pattern. Also, the curves of PINN and FEA overlap at every time point. For t = 50 s, the

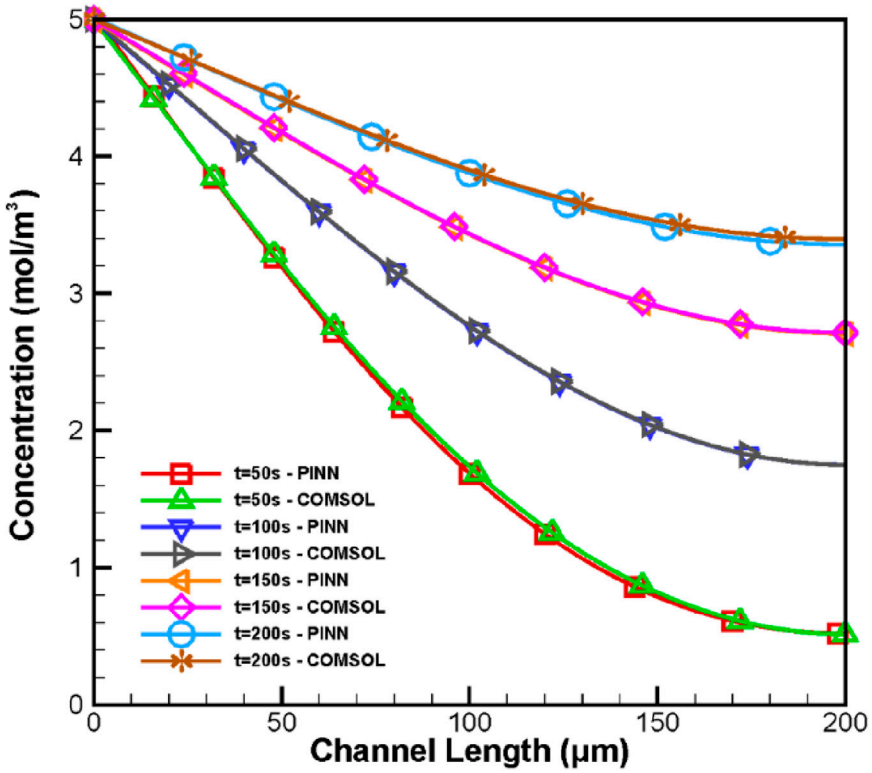

FIGURE 9
The concentration distributions for pressure-driven flow.

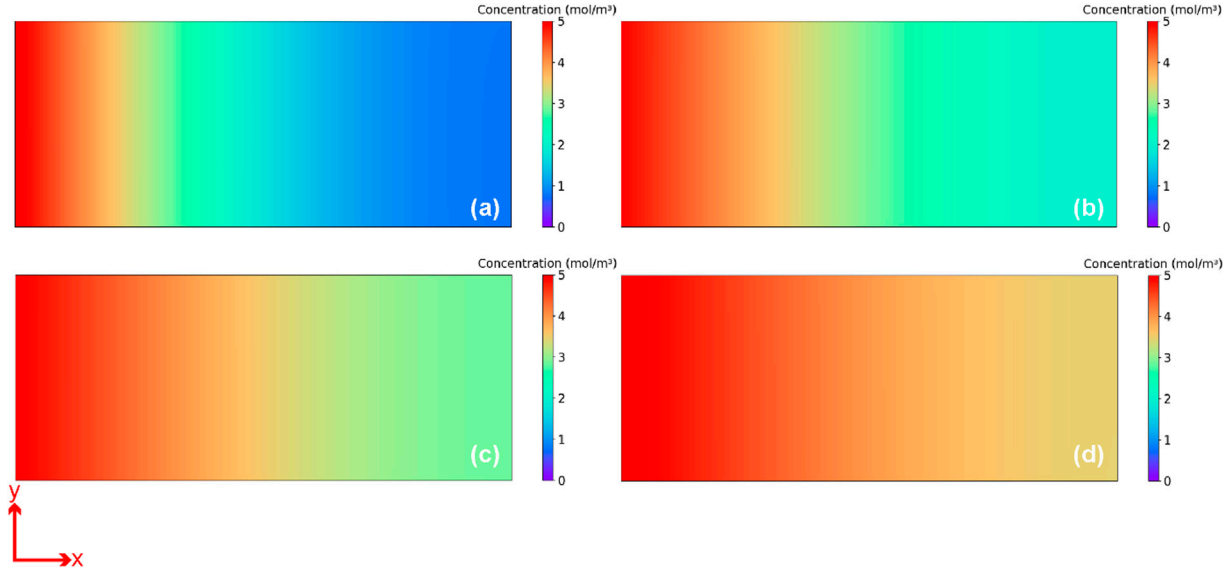

FIGURE 10
Chemical species transport under electrokinetically-driven flow conditions for the moments of **(a)** t = 50 s **(b)** t = 100 s **(c)** t = 150 s **(d)** 200 s.

largest deviation is observed between the PINN and FEA, especially adjacent to the outlet. Inlet concentration is always calculated as C_0 = 5 mol/m^3, due to the invariable nature of the predefined boundary concentration. On the contrary, the outlet concentrations are varied as C = 0.72 mol/m^3, C = 1.93 mol/m^3, C = 2.83 mol/m^3 and C = 3.46 mol/m^3 for t = 50–100-150–200 s, respectively. Correspondence of these values is calculated by COMSOL Multiphysics, such as C = 0.55 mol/m^3, C = 1.85 mol/m^3,

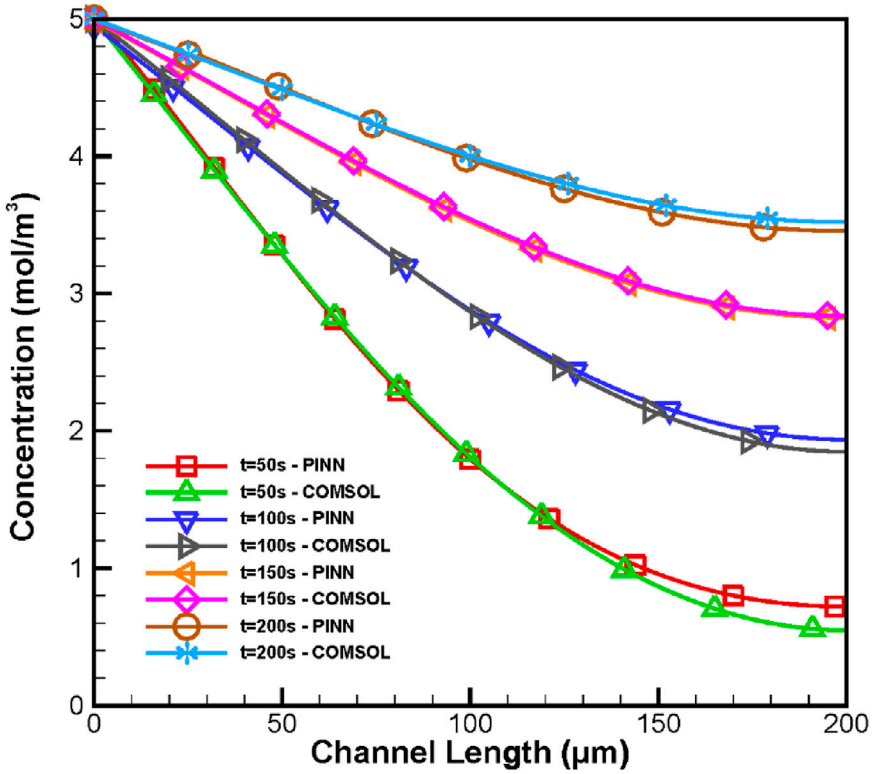

FIGURE 11
The concentration distributions for electroosmotic flow.

C = 2.84 mol/m^{3,} and C = 3.52 mol/m^3 for t = 50–100-150–200 s, respectively. Most deviation is observed at the outlet, which is 30% higher than that of PINN. However, RMSE values are calculated as adequately low, such as 0.077–0.048–0.014–0.042 t = 50–100-150–200 s, respectively. All aforementioned RMSE values for the related problems are lower than 0.1, which can be considered as fairly acceptable while the concentration interval is between 0 and 5. Besides, low RMSE values for pressure-driven and electrokinetically-driven flows are another proof for consistency between the analyses of steady and time-dependent of Navier-Stokes Equations.

4 Conclusions

In the present study, the transport of fluid and species along a straight microchannel is presented using physics-informed neural networks (PINN) for Reynolds numbers within a range of $5 \times 10^{-6} \leq Re \leq 5 \times 10^{-2}$. For this purpose, Navier-Stokes and Nernst-Planck equations are solved simultaneously with PINN, in which the velocity term is determined as the coupling parameter between these equations. The models are initially defined as steady, and the fluid and species transport are investigated in a microscale domain under pressure-driven and electroosmotic flow conditions. The predefined models are modified to be time-dependent for these flow conditions. Each calculated data point is compared with the outcomes of a solver for finite element analysis (FEA), COMSOL Multiphysics. Since the Navier-Stokes equation remains steady to alleviate the computational burden of PINN, its time-dependent form is implemented in FEA. Moreover, the pressure scale for PINN must be determined according to the inlet pressure to achieve reasonable loss values. It is observed that PINN and FEA solvers are in alignment for all conditions under the steady and time-dependent states. This significant overlap between the two solvers is quantitatively expressed with RMSE values. RMSE values for concentration profiles are determined as 0.001 and 0.003 for steady pressure-driven and electroosmotic flows, respectively. RMSE values of concentration profiles are separately calculated at t = 50–100-150–200 s for time-dependent problems, which are 0.033, 0.005, 0.006, and 0.025, and 0.077, 0.048, and 0.014 for pressure-driven flow and electrokinetically-driven flow, respectively. Therefore, the steady Navier-Stokes equation can be safely utilized instead of the time-dependent one for fluid flow problems. The slightly higher RMSE of the electrokinetics can be attributed to the inclusion of one more dependent variable. In conclusion, PINN provides a suitable alternative for solving fluid and mass transport problems along a microchannel under current conditions.

Data availability statement

The raw data supporting the conclusions of this article will be made available by the authors, without undue reservation.

Author contributions

MT: Conceptualization, Data curation, Formal Analysis, Investigation, Methodology, Software, Visualization, Writing – original draft, Writing – review and editing. CC: Conceptualization, Formal Analysis, Funding acquisition, Methodology, Project administration, Resources, Supervision, Writing – original draft, Writing – review and editing.

Funding

The author(s) declared that financial support was received for this work and/or its publication. This work is supported financially by Cukurova University Scientific Research Office under contact numbers FBA-2025-17180 and FDK-2023-15643.

Conflict of interest

The author(s) declared that this work was conducted in the absence of any commercial or financial relationships that could be construed as a potential conflict of interest.

Generative AI statement

The author(s) declared that generative AI was not used in the creation of this manuscript.

Any alternative text (alt text) provided alongside figures in this article has been generated by Frontiers with the support of artificial intelligence and reasonable efforts have been made to ensure accuracy, including review by the authors wherever possible. If you identify any issues, please contact us.

Publisher's note

Supplementary material

The Supplementary Material for this article can be found online at: https://www.frontiersin.org/articles/10.3389/fmech.2025.1651334/full#supplementary-material

References

Abohtyra, R., Chait, Y., Germain, M. J., Hollot, C. V., and Horowitz, J. (2019). Individualization of ultrafiltration in hemodialysis. *IEEE Trans. Biomed. Eng.* 66, 2174–2181. doi:10.1109/TBME.2018.2884931

Agnaou, M., Sadeghi, M. A., Tranter, T. G., and Gostick, J. T. (2020). Modeling transport of charged species in pore networks: solution of the nernst–planck equations coupled with fluid flow and charge conservation equations. *Comput. Geosci.* 140, 104505. doi:10.1016/J.CAGEO.2020.104505

Ai, Y., Joo, S. W., Jiang, Y., Xuan, X., and Qian, S. (2009). Transient electrophoretic motion of a charged particle through a converging–diverging microchannel: effect of direct current-dielectrophoretic force. *Electrophoresis* 30, 2499–2506. doi:10.1002/ELPS.200800792

Al-Safran, E., Aql, A., and Nguyen, T. (2017). Analysis and prediction of fluid flow behavior in progressing cavity pumps. *J. Fluids Eng. Trans. ASME* 139, 121102. doi:10.1115/1.4037057/371959

Andar, A. U., Hood, R. R., Vreeland, W. N., Devoe, D. L., and Swaan, P. W. (2014). Microfluidic preparation of liposomes to determine particle size influence on cellular uptake mechanisms. *Pharm. Res.* 31, 401–413. doi:10.1007/S11095-013-1171-8/FIGURES/7

Andrews, A. J., Bühlmann, P., and Hogan, C. J. (2023). Determination of forced convection effects on the response of membrane-based ion-selective electrodes via numerical solution to the Navier-Stokes-Nernst-Plank-Poisson equations. *Chem. Eng. Sci.* 282, 119275. doi:10.1016/J.CES.2023.119275

Bai, X. D., and Zhang, W. (2022). Machine learning for vortex induced vibration in turbulent flow. *Comput. Fluids* 235, 105266. doi:10.1016/J.COMPFLUID.2021.105266

Canpolat, C., Qian, S., and Beskok, A. (2013a). Micro-PIV measurements of induced-charge electro-osmosis around a metal rod. *Microfluid Nanofluidics* 14, 153–162. doi:10.1007/s10404-012-1033-4

Canpolat, C., Zhang, M., Rosen, W., Qian, S., and Beskok, A. (2013b). Induced-charge electroosmosis around touching metal rods. *J. Fluids Eng.* 135, 021103. doi:10.1115/1.4023452

Constantin, P., Ignatova, M., and Lee, F. N. (2021). Nernst–planck–Navier–stokes systems far from equilibrium. *Arch. Ration. Mech. Anal.* 240, 1147–1168. doi:10.1007/S00205-021-01630-X/METRICS

Das, P. K., Snider, A. D., and Bhethanabotla, V. R. (2019). Acoustothermal heating in surface acoustic wave driven microchannel flow. *Phys. Fluids* 31, 106106. doi:10.1063/1.5121307/15961547/106106_1_ACCEPTED_MANUSCRIPT

de Rutte, J. M., Janssen, K. G. H., Tas, N. R., Eijkel, J. C. T., and Pennathur, S. (2016). Numerical investigation of micro- and nanochannel deformation due to discontinuous electroosmotic flow. *Microfluid Nanofluidics* 20, 1–12. doi:10.1007/S10404-016-1815-1/TABLES/1

De Ryck, T., Lanthaler, S., and Mishra, S. (2021). On the approximation of functions by tanh neural networks. *Neural Netw.* 143, 732–750. doi:10.1016/J.NEUNET.2021.08.015

Fadhil Majnis, M., Francis, H., and Zilati Ku Shaari, K. (2018). Droplet formation in microchannels at low values of the capillary and the reynolds numbers. *Mater Today Proc.* 5, 21765–21771. doi:10.1016/J.MATPR.2018.07.030

Hu, B., and McDaniel, D. (2023). Applying physics-informed neural networks to solve navier–stokes equations for laminar flow around a particle. *Math. Comput. Appl.* 28, 102–128. doi:10.3390/MCA28050102

Huang, N., Han, S., Zhang, X., Wang, G., and Jiang, Y. (2024). Effects of surface roughness and reynolds number on the solute transport through three-dimensional rough-walled rock fractures under different flow regimes. *Sci. Rep.* 14 (14), 1–23. doi:10.1038/s41598-024-73011-9

Hur, J., Park, I., Lim, K. M., Doh, J., Cho, S. G., and Chung, A. J. (2020). Microfluidic cell stretching for highly effective gene delivery into hard-to-transfect primary cells. *ACS Nano* 14, 15094–15106. doi:10.1021/ACSNANO.0C05169/SUPPL_FILE/NN0C05169_SI_008.MOV

Insepov, Z., Ramazanova, Z., Zhakiyev, N., and Tynyshtykbayev, K. (2021). Water droplet motion under the influence of surface acoustic waves (SAW). *J. Phys. Commun.* 5, 035009. doi:10.1088/2399-6528/ABDA13

Jalili, D., Jang, S., Jadidi, M., Giustini, G., Keshmiri, A., and Mahmoudi, Y. (2024). Physics-informed neural networks for heat transfer prediction in two-phase flows. *Int. J. Heat. Mass Transf.* 221, 125089. doi:10.1016/J.IJHEATMASSTRANSFER.2023.125089

Kingma, D. P., and Ba, J. L. (2014). Adam: a method for stochastic optimization. In: 3rd international conference on learning representations, ICLR 2015 - conference track proceedings; 2015 May 7-9; San Diego, CA, USA. Available online at: https://arxiv.org/pdf/1412.6980 (Accessed September 1, 2025).

Laurila, E., Roenby, J., Maakala, V., Peltonen, P., Kahila, H., and Vuorinen, V. (2019). Analysis of viscous fluid flow in a pressure-swirl atomizer using large-eddy simulation. *Int. J. Multiph. Flow* 113, 371–388. doi:10.1016/J.IJMULTIPHASEFLOW.2018.10.008

Lauser, A., Hager, C., Helmig, R., and Wohlmuth, B. (2011). A new approach for phase transitions in miscible multi-phase flow in porous media. *Adv. Water Resour.* 34, 957–966. doi:10.1016/J.ADVWATRES.2011.04.021

Lu, L., Meng, X., Mao, Z., and Karniadakis, G. E. (2021). DeepXDE: a deep learning library for solving differential equations. *SIAM Rev. Soc. Ind. Appl. Math.* 63, 208–228. doi:10.1137/19M1274067

Mao, M., Sherwood, J. D., and Ghosal, S. (2014). Electro-osmotic flow through a nanopore. *J. Fluid Mech.* 749, 167–183. doi:10.1017/JFM.2014.214

Meagher, R. J., Hatch, A. V., Renzi, R. F., and Singh, A. K. (2008). An integrated microfluidic platform for sensitive and rapid detection of biological toxins. *Lab. Chip* 8, 2046–2053. doi:10.1039/B815152K

Musbah, H., Aly, H. H., and Little, T. A. (2021). Energy management of hybrid energy system sources based on machine learning classification algorithms. *Electr. Power Syst. Res.* 199, 107436. doi:10.1016/J.EPSR.2021.107436

Namnabat, M. S., Moghimi Zand, M., and Houshfar, E. (2021). 3D numerical simulation of acoustophoretic motion induced by boundary-driven acoustic streaming in standing surface acoustic wave microfluidics. *Sci. Rep.* 11 (11), 1–16. doi:10.1038/s41598-021-90825-z

Noori, M. S., Taleghani, A. S., and Rahni, M. T. (2021). Surface acoustic waves as control actuator for drop removal from solid surface. *Fluid Dyn. Res.* 53, 045503. doi:10.1088/1873-7005/AC12AF

Oldenburg, J., Wollenberg, W., Borowski, F., Schmitz, K. P., Stiehm, M., and Öner, A. (2023). Augmentation of experimentally obtained flow fields by means of physics Informed neural networks (PINN) demonstrated on aneurysm flow. *Curr. Dir. Biomed. Eng.* 9, 519–523. doi:10.1515/CDBME-2023-1130/MACHINEREADABLECITATION/RIS

Paik, K. H., Liu, Y., Tabard-Cossa, V., Waugh, M. J., Huber, D. E., Provine, J., et al. (2012). Control of DNA capture by nanofluidic transistors. *ACS Nano* 6, 6767–6775. doi:10.1021/NN3014917/SUPPL_FILE/NN3014917_SI_001

Rafati, J., and Marica, R. F. (2020). Quasi-newton optimization methods for deep learning applications. *Adv. Intelligent Syst. Comput.* 1098, 9–38. doi:10.1007/978-981-15-1816-4_2

Raissi, M., Perdikaris, P., and Karniadakis, G. E. (2019). Physics-informed neural networks: a deep learning framework for solving forward and inverse problems involving nonlinear partial differential equations. *J. Comput. Phys.* 378, 686–707. doi:10.1016/J.JCP.2018.10.045

Reinmüller, A., Schöpe, H. J., and Palberg, T. (2013). Self-organized cooperative swimming at low reynolds numbers. *Langmuir* 29, 1738–1742. doi:10.1021/LA3046466/SUPPL_FILE/LA3046466_SI_005.MPG

Sarioglu, A. F., Aceto, N., Kojic, N., Donaldson, M. C., Zeinali, M., Hamza, B., et al. (2015). A microfluidic device for label-free, physical capture of circulating tumor cell clusters. *Nat. Methods* 12 (7), 685–691. doi:10.1038/nmeth.3404

Singh, A. R., Rohr, B. A., Gauthier, J. A., and Nørskov, J. K. (2019). Predicting chemical reaction barriers with a machine learning model. *Catal. Lett.* 149, 2347–2354. doi:10.1007/S10562-019-02705-X/FIGURES/5

Tatlısoz, M. M., and Canpolat, Ç. (2018). Pulsatile flow micromixing coupled with ICEO for Non-Newtonian fluids. *Chem. Eng. Process. - Process Intensif.* 131, 12–19. doi:10.1016/J.CEP.2018.07.002

Tsuboi, N., Matsumoto, S., Nishimura, N., Nakagawa, S., and Kobayashi, H. (2019). Fluid dynamics approach to airway obstruction. *Med. Hypotheses* 132, 109341. doi:10.1016/J.MEHY.2019.109341

Wu, Y. A., Panigrahi, B., Lu, Y. H., and Chen, C. Y. (2017). An integrated artificial cilia based microfluidic device for micropumping and micromixing applications. *Micromachines* 8, 260–268. doi:10.3390/MI8090260

Xiao, L. L., Song, X. J., and Chen, S. (2021). Motion of a tumour cell under the blood flow at low reynolds number in a curved microvessel. *Mol. Simul.* 47, 1–9. doi:10.1080/08927022.2020.1856377

Yang, B., Lei, Y., Li, N., Li, X., Si, X., and Chen, C. (2025). Balance recovery and collaborative adaptation approach for federated fault diagnosis of inconsistent machine groups. *Knowl. Based Syst.* 317, 113480. doi:10.1016/J.KNOSYS.2025.113480

Yuan, S., Zhou, M., Liu, X., and Jiang, B. (2023). Effect of pressure-driven flow on electroosmotic flow and electrokinetic mass transport in microchannels. *Int. J. Heat. Mass Transf.* 206, 123925. doi:10.1016/J.IJHEATMASSTRANSFER.2023.123925

Nomenclature

t	Time variable
x	Location variable for the horizontal axis
y	Location variable for the vertical axis
L	Length of the microchannel and length scale
W	Width of the microchannel
V	Fluid velocity
u	x-velocity
v	y-component of the fluid velocity
ρ	Fluid density
μ	Fluid viscosity
p	Pressure
$\mathbf{P_{in}}$	Inlet pressure
$\mathbf{P_{out}}$	Outlet pressure
F	Body force
Φ	Electrical potential difference
$\boldsymbol{\phi_{in}}$	Inlet electrical potential difference
$\mathbf{u_{eow}}$	Smoluchowski slip velocity in the -x direction
ε	Electrical permittivity of the medium
$\boldsymbol{\zeta_w}$	Zeta potential of the microchannel walls
$\mathbf{E_t}$	The tangential component of the electrical field
C	Concentration
$\mathbf{C_0}$	Inlet concentration
D	Diffusion coefficient
σ	Activation function of the neural network
$\mathbf{t_{scale}}$	Scaling factor for time term
$\mathbf{L_{scale}}$	Scaling factor for length terms
$\mathbf{u_{scale}}$	Scaling factor for velocity term
$\mathbf{p_{scale}}$	Scaling factor for pressure term
$\mathbf{C_{scale}}$	Scaling factor for concentration term
$\boldsymbol{\phi_{scale}}$	Scaling factor for electric potential term
t*	Dimensionless time variable
x*	Dimensionless horizontal location variable
y*	Dimensionless vertical location variable
V*	Dimensionless velocity
u*	Dimensionless x-velocity
p*	Dimensionless pressure
C*	Dimensionless concentration
ϕ*	Dimensionless electric potential
2D	2-dimensional
Re	Reynolds number
Pe	Peclet number
EDL	Electrical double layer
FEA	Finite element analysis
L	Loss term of the neural network
$\mathbf{MSE_f}$	Mean-squared error of the partial differential equation
$\mathbf{MSE_b}$	Mean-squared error of the boundary condition
$\mathbf{MSE_{init}}$	Mean-squared error of the initial condition
$f(t^{*i}_f, x^{*i}_f, y^{*i}_f)$	Calculated values of the partial differential equation
$\tilde{u}(t^{*i}_f, x^{*i}_f, y^{*i}_f)$	Calculated values of the boundary condition
$\bar{\bar{u}}(t^{*i}_f, x^{*i}_f, y^{*i}_f)$	Calculated values of the initial condition
$\tilde{u}$	The exact value of the boundary condition
$\bar{\bar{u}}$	The exact value of the initial condition